

## Chapter 2

# Materials and Experimental Techniques

This chapter discusses the different preparation and characterization techniques that were used during this work. In Sect. 2.1 we focus on the materials and the deposition techniques that were exploited. In addition the fabrication of nanostructured substrates is briefly discussed. The different techniques that were used to characterize the samples are subject of Sect. 2.2.

### 2.1 Sample Fabrication

#### 2.1.1 Materials Used in this Work

The molecular formulas of the organic materials that were used in this work are represented in Fig. 2.1. The correct chemical designation of each organic compound can be found in Table 2.1. PTCDI- $C_{13}H_{27}$ , Alq<sub>3</sub>, P $\alpha$ Ms, COT and anthracene, were purchased from Sigma-Aldrich, CNPPP and DCM<sub>2</sub> from H.W. Sands Corp., DFH-4T and DFHCO-4T from Polyera Corp. and Btp<sub>2</sub>Ir(acac) from American Dye Source Inc. PTAA is received from Merck, whereas F5Ph and GDP16b came from the group of Prof. L. De Cola. MeLPPP and PF2/6 were synthesized by the group of Prof. U. Scherf. Most of these materials were used as received. Only PTCDI- $C_{13}H_{27}$  and Alq<sub>3</sub> were purified once by train sublimation before loading into an ultra-high vacuum system ( $p = 10^{-8}$  torr). The lowest unoccupied molecular orbital (LUMO) and the highest occupied molecular orbital (HOMO) of most of these molecules are depicted in Fig. 2.2.

Prior to the deposition of organic materials, the substrates were cleaned with solvents (acetone and isopropanol) and exposed to an UV-ozone ambient for 15 minutes. Processing steps after UV-ozone treatment were usually carried out in a dry N<sub>2</sub> glovebox (<1 ppm O<sub>2</sub>, <5 ppm H<sub>2</sub>O) or in ultra-high vacuum. Both systems are attached to each other, making transport of samples from high-vacuum to the glovebox and vice versa possible without exposure to ambient atmosphere.

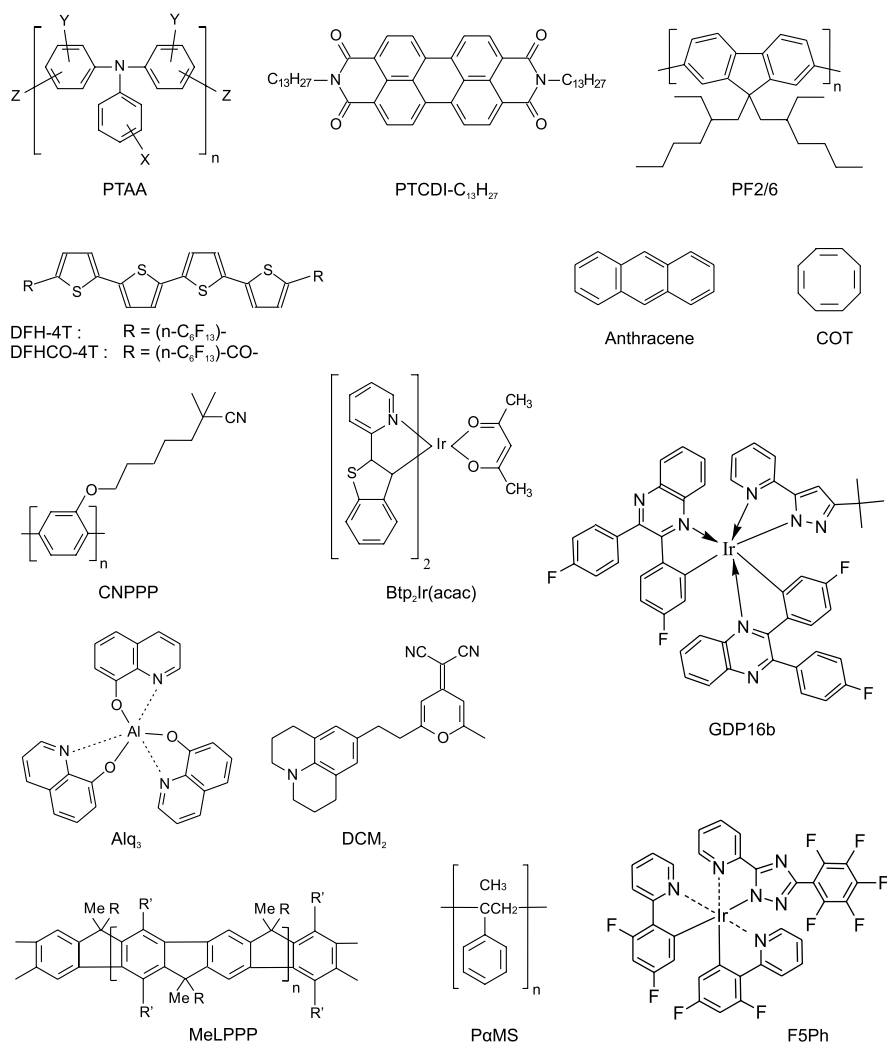


**Fig. 2.1** The molecular structure of the organic materials used in this work

### 2.1.2 Deposition Techniques

Organic semiconductor films can be fabricated using various deposition techniques. If the molecule is soluble in an organic solvent, deposition techniques such as spin-coating, drop-casting, spray-coating and inkjet-printing can be used. Polymer semiconductors are usually deposited in this way. Organic small molecules on the other hand, are generally not very soluble in common solvents and are therefore typically deposited using organic molecular beam deposition (OMBD) or by organic vapor deposition. In these techniques the organic material is heated above the evaporation

**Table 2.1** Chemical description of the organic compounds shown in Fig. 2.1

| Abbreviation                          | Chemical description   |
|---------------------------------------|--|
| Alq <sub>3</sub>                      | tris(8-hydroxyquinoline) aluminum  |
| Btp <sub>2</sub> Ir(acac)             | bis(2-(2'-benzothienyl)pyridinato-N,C <sup>3'</sup> )(acetylacetonate)iridium(III)             |
| CNPPP                                 | 2-[(6-Cyano-6-methylheptyloxy)-1,4-phenylene] copolymer  |
| COT                                   | 1,3,5,7-cyclooctatetraene  |
| DCM <sub>2</sub>                      | 4-(Dicyanomethylene)-2-methyl-6-(julolindin-4-yl-vinyl)-4H-pyran                               |
| DFH-4T                                | $\alpha,\omega$ -diperfluorohexyl-quaterthiophene  |
| DFHCO-4T                              | 5, 5'''-diperfluorohexylcarbonyl-2,2':5'',2''':5'',2'''-quaterthiophene                        |
| F5Ph                                  | bis((2,4-difluoro)phenylpyridine)-(2-(1,2,4-triazol-3-pentafluorophenyl)-pyridine)iridium(III) |
| GDP16b                                | 2,3-Bis(4-fluorophenyl)quinoxaline(3-tert-butyl-5-(2-pyridyl)pyrazole)-iridium(III)            |
| MeLPPP                                | methyl-substituted ladder-type poly(para-phenylene)  |
| P $\alpha$ Ms                         | poly- $\alpha$ -methylstyrene  |
| PF2/6                                 | poly(9,9-di(ethylhexyl)fluorene)   |
| PTAA                                  | Poly(triarylamine)   |
| PTCDI-C <sub>13</sub> H <sub>27</sub> | N,N'-ditridecylperylene-3,4,9,10-tetracarboxylic diimide                                       |

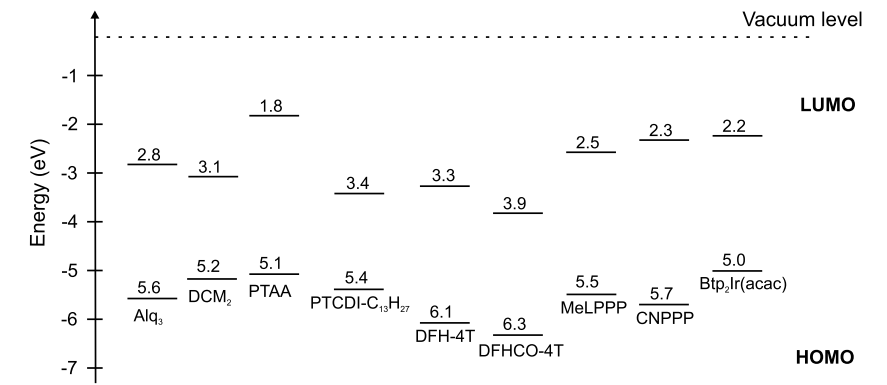


**Fig. 2.2** The HOMO and LUMO energy levels of most organic semiconducting materials used in this work [235–240]

temperature and transported towards the substrate in vacuum or with a carrier gas. In this work organic thin-films were prepared using OMBD or spin-coating. Both techniques will be briefly discussed below.

**Table 2.2** Typical processing conditions for the organic compounds of Fig. 2.1 that were deposited via spin-coating

| abbreviation  | concentration<br>mg/ml | spin-speed<br>(rpm) | $T_{bake}$<br>(°C) | thickness<br>(nm) |
|---------------|------------------------|---------------------|--------------------|-------------------|
| CNPPP         | 10 (chlorobenzene)     | 1000                | –                  | 100               |
| MeLPPP        | 15 (toluene)           | 1000                | –                  | 150               |
| P $\alpha$ Ms | 0.86 (toluene)         | 4000                | 120 (1 min.)       | 5                 |
| PF2/6         | 10 (toluene)           | 1000                | –                  | 100               |
| PTAA          | 45 (toluene)           | 1000                | 110 (20 min.)      | 50                |

## Spin-Coating

The most commonly used deposition technique for soluble organic semiconductors is spin-coating. The substrate, which is centered on the chuck of a spin-coater, is covered with a solution containing the dissolved organic compound. Upon revolving the sample, centrifugal force spins off the fluid and a uniform film is created. Afterwards, the persistent solvent can be removed by baking the sample on a hotplate at elevated temperatures. The resulting film thickness depends on the molecular weight of the organic material, the concentration of the solution and the spin-speed. For the organic compounds of Fig. 2.1 that were deposited by spin-coating, the typically used concentration, solvent, spin-speed, baking temperature  $T_{bake}$  and the resulting film thickness are summarized in Table 2.2. The layer thickness was determined using a Veeco Dektak V200-Si stage profiler or by spectroscopic ellipsometry (Sopra GESp-5).

## Organic Molecular Beam Deposition

A disadvantage of solution processing is the fact that the fabrication of heterostructures is limited by the demand for orthogonal solvents. This problem can be circumvented by deposition of the organic compounds by OMBD. OMBD is a standard technique to deposit small molecular weight organic materials. The organic material is loaded into a (ultra) high vacuum chamber inside a container (boat or crucible) which can be heated. When the organic material is heated above its evaporation temperature, molecules are sublimed from the container. The molecular beam is directed towards the substrate, where molecules can condense and form a layer. In this way, films of only a few monolayers up to micrometers thickness can be obtained with high accuracy. Depending on the deposition conditions (deposition flux and substrate temperature) the growth of the organic materials can be controlled and an amorphous or polycrystalline film is formed.

At imec, four ultra-high vacuum chambers ( $p = 10^{-8}$  torr) are available for OMBD of organic materials and evaporation of metals. The four chambers are connected to a central transfer chamber, which is for his part connected to a N<sub>2</sub>-filled glovebox by means of a loadlock. Each of the four evaporation chambers is equipped

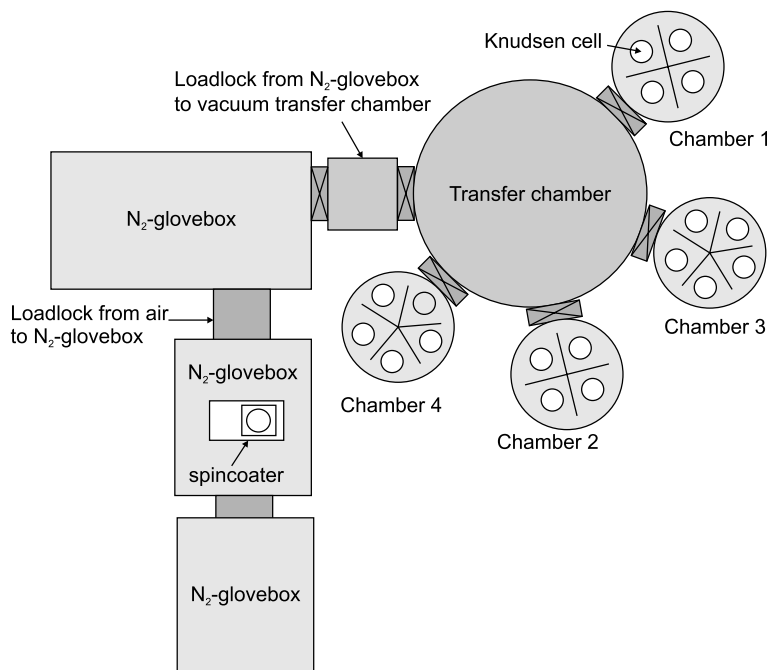


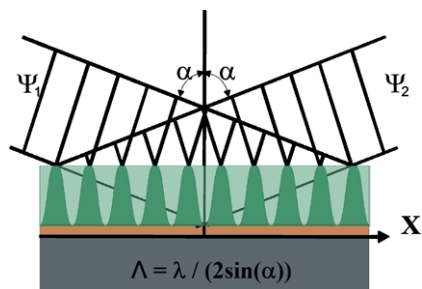
**Fig. 2.3** Ultra-high vacuum cluster system with attached  $N_2$  gloveboxes for vacuum deposition of organic materials and metals

with several Knudsen cells, containing a crucible filled with an organic material or a metal. The deposition rate can be controlled by the temperature of the Knudsen cell and is in-situ measured by a calibrated water-cooled quartz crystal monitor. The temperature of the substrate can also be independently controlled. Every cell has a shutter that can be used to block the evaporated material flux. In addition, the flux reaching the substrate can be blocked by another shutter located close to the substrate itself, which is particularly useful to calibrate the deposition rate. PTCDI- $C_{13}H_{27}$ ,  $Alq_3$ ,  $DCM_2$ , DFH-4T, DFHCO-4T,  $Btp_2Ir(acac)$  and GDP16b were typically deposited using OMBD. A schematical illustration of the ultra-high vacuum cluster system available at imec is shown in Fig. 2.3.

### 2.1.3 Fabrication of Photonic Feedback Structures

As described in Chap. 1 (Sect. 1.3.3) low threshold organic semiconductor lasers can be obtained using diffractive resonator structures. Distributed feedback relies on a periodic modulation of the refractive index or the gain of the active material and can be achieved by corrugating the substrate with a periodic height modulation. In close collaboration with IBM Research Zurich and AMO GmbH in Aachen different photonic feedback structures have been fabricated. For structure definition two main

**Fig. 2.4** Schematic illustration of 2-beam interference lithography. An interference pattern between two coherent light waves is transferred to a photoresist layer



lithography technologies have been used: first, large area gratings have been realized by interference lithography (IL) and second, for sub 100 nm resolution in dense structures electron beam lithography (EBL) has been performed.

### Fabrication of Linear Gratings Using Interference Lithography

Interference lithography is a technique for patterning regular arrays of fine features, without the use of complex optical systems or photolithography masks. The basic principle is the same as in interferometry or holography. An interference pattern between two or more coherent light waves is set up and recorded in a layer (photoresist). This interference pattern consists of a periodic series of fringes representing intensity minima and maxima. Upon post-exposure photolithographic processing, a photoresist pattern corresponding to the periodic intensity pattern emerges. For 2-beam interference, as depicted in Fig. 2.4, the period is given by  $\lambda / (2 \sin(\alpha))$ , where  $\lambda$  is the wavelength and  $\alpha$  is the angle between the interfering wave and the substrate normal. The minimum period achievable is half of the wavelength.

Large area linear gratings have been realized with laser interference lithography. Typically, the exposures were carried out on 1.8  $\mu\text{m}$  thick  $\text{SiO}_2$  layers thermally grown on Si substrates. On top of these substrates a two layer resist, consisting of a bottom anti reflection coating (BARC) layer to suppress substrate reflectance and a chemical amplified resist, was deposited. Exposure was performed at a wavelength of 266 nm and by exact adjustment of the exposure dose the desired line width of the grating could be achieved. In this way, different gratings with different line width and period could be realized. A scanning electron microscopy image (SEM) of the resist structure of a linear grating (line width 160 nm and period 325 nm) after development is shown in Fig. 2.5.

After lithography the resist pattern was transferred into the  $\text{SiO}_2$  by dry etching. An inductively coupled plasma reactive ion etching (ICP-RIE) tool was used to perform this etching. In a first step, the BARC layer of the samples exposed by IL was etched using  $\text{O}_2$  plasma. Next, an etching process based on  $\text{C}_4\text{F}_8$ <sup>1</sup> and helium (He) chemistry made it possible to transfer the lithographically defined structures into

<sup>1</sup>Octafluorocyclobutane.

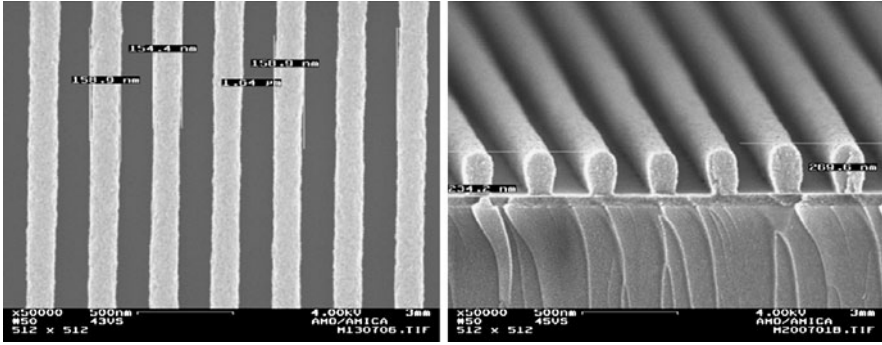


**Fig. 2.5** Top view (*left*) and cross-sectional view (*right*) SEM images of 160 nm wide lines realized by IL. (Images received from AMO GmbH)

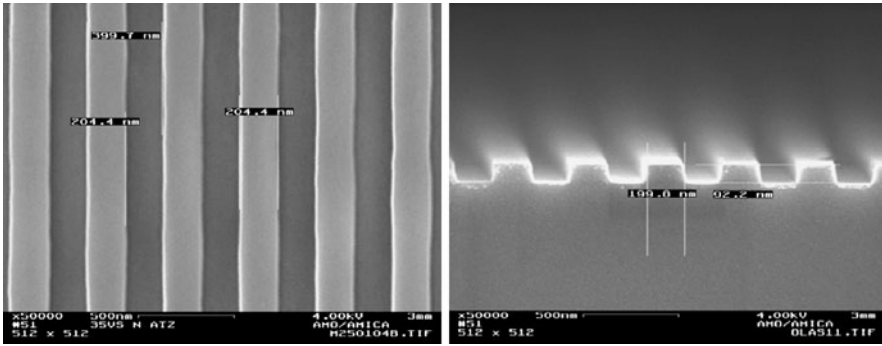


**Fig. 2.6** (*Left*) Top view SEM micrograph of a fully fabricated linear grating resonators in SiO<sub>2</sub>, and (*right*) cross-sectional SEM image of the same grating. The 90 nm deep trenches exhibit a profile angle of better than 80°. (Images received from AMO GmbH)

the SiO<sub>2</sub> layer. Depending on the actual design of the pattern a precise adjustment of many process parameters like ICP/RF power, C<sub>4</sub>F<sub>8</sub>/He mixture, etching temperature etc. was necessary to achieve a satisfying etching result. As an example for the dimensional stability of the optimized etching process a SEM micrograph of a completely fabricated grating is shown in Fig. 2.6 (left). The grating had a desired line width of 200 nm. The deviation between the designed pattern size and the realized pattern size is in the range of a few nm. This demonstrates the potential of IL and ICP etching to fabricate defined linear gratings with a line width accuracy of a few nm. Further, IL allows the fast production of large area gratings with a wide range of line widths ranging from 80 nm to 500 nm. This flexibility makes IL an ideal lithography technology for testing different materials and different grating structures. Besides the dimensional stability between the lithographic and the etched structures, the steepness of the etched trenches is also an important parameter, defining the quality of the etching process. To determine the profile of the gratings the cross-section has been investigated using SEM. Figure 2.6 (right) shows the cross-

sectional SEM image of the grating displayed in Fig. 2.6 (left). A profile angle of better than  $80^\circ$  could be determined.

### Fabrication of Linear Gratings Using Electron Beam Lithography

Although IL is a powerful technique that allows fast fabrication of large area gratings, other technologies with higher contrast are mandatory for sub 100 nm resolution. Electron beam lithography (EBL) was used in this case. Exposure was performed at AMO GmbH with a Leica EBPG5000 system. To ensure accurate electron beam lithography on the insulating substrates a 40 nm thick Ti layer was deposited as intermediate layer between the  $\text{SiO}_2$  surface and the electron sensitive resist. The Ti layer prevented charging during the exposure and acted as a hard mask for the following etching processes. To resolve fine structures an EBL process with high contrast value is necessary. The negative tone electron sensitive resist HSQ<sup>2</sup>, pre-baked at moderate temperature, fulfils this requirement. The resist was spin-coated on top of the substrate resulting in a thickness of about 200 nm, which is sufficient to act as an efficient etching mask. After electron beam exposure the development was carried out in highly concentrated TMAH<sup>3</sup>. As shown in Fig. 2.7 (left), clearly resolved 80 nm trenches between 240 nm wide lines can be obtained in this way. Figure 2.7 (right) shows the cross-section of a developed HSQ pattern. The steep resist structures without any broadening at the foot of the line demonstrate its high quality.

Using the 200-nm thick HSQ pattern as an etch mask, the structures could then be transferred into the  $\text{SiO}_2$  substrate using the same ICP-RIE tool as for the samples exposed by IL. First, a  $\text{BCl}_3$ <sup>4</sup> chemistry based etching process was performed to etch

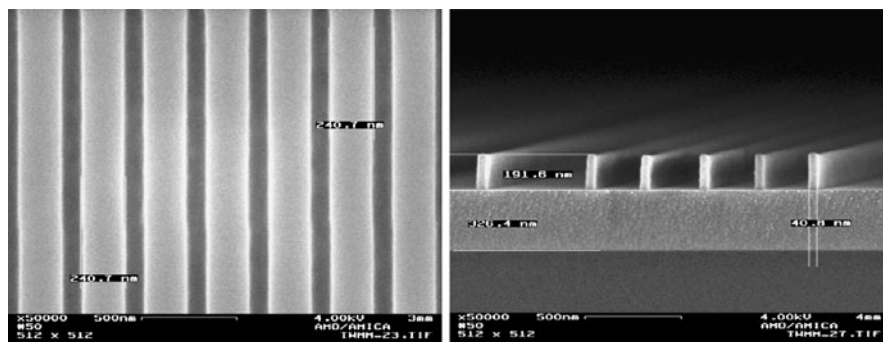


**Fig. 2.7** (Left) Top view SEM image of a linear grating in HSQ with line to space ratio of 1:3, and (right) Cross sectional SEM image of a HSQ resist pattern. (Images received from AMO GmbH)

<sup>2</sup>Hydrogen silsesquioxane.

<sup>3</sup>Tetramethylammonium hydroxide.

<sup>4</sup>Boron trichloride.



the Ti layer. Second, the main etching process based on  $C_4F_8$  and He chemistry was applied.

## 2.2 Device Characterization

After fabrication the samples and devices were characterized using various techniques. Basic characterization was performed using atomic force microscopy, ellipsometry, transmission spectroscopy and absorption measurements. Some other measurement techniques used to characterize our samples are briefly discussed in this section.

### 2.2.1 Transistor Measurement and Parameter Extraction

The electrical characteristics of organic thin-film transistors were measured in an inert  $N_2$  atmosphere using an Agilent 4156C parameter analyzer. Standard x-y-z control probes (Karl Suss, PH120) were used to connect three source-measure units (SMU) to the device. Two major types of transistor measurements were usually performed. First, the transistor output characteristics were measured, meaning that a fixed gate voltage was applied to the gate electrode, while varying the drain voltage. This results in  $I_{ds}-V_{ds}$  measurements for different gate voltages as illustrated in Fig. 2.8(a) for an  $n$ -type organic thin-film transistor. Two regimes can be distinguished: the linear regime, where  $I_{ds}$  increases with  $V_{ds}$ , and the saturation regime, where  $I_{ds}$  is almost independent of  $V_{ds}$ . Second, the  $I_{ds}-V_{gs}$  or transfer characteristics were measured. This type of experiment measures the drain current as a function of the gate voltage. Depending on the value of the drain voltage, the transistor operates either in the linear or in the saturation regime during the measurement. An

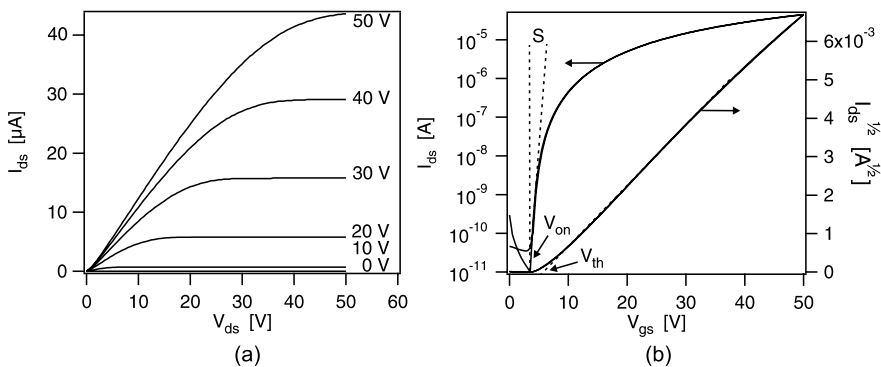


**Fig. 2.8** (a) Typical output characteristics, and (b) transfer characteristics of an  $n$ -channel organic thin-film transistor with PTCDI- $C_{13}H_{27}$  as the organic semiconductor ( $W/L = 2000/130$ )

example of a transistor transfer characteristic, measured in the saturation regime is shown in Fig. 2.8(b).

The transfer characteristics are very useful for extracting the basic transistor parameters. Assuming the gradual channel approximation, the current-voltage characteristics can be analytically described by:

$$I_{ds} = \frac{W}{L} \mu C_{ox} \left( V_{gs} - V_{th} - \frac{V_{ds}}{2} \right) V_{ds} \quad (|V_{ds}| < |V_{gs} - V_{th}|), \quad (2.1)$$

$$I_{ds} = \frac{W}{2L} \mu C_{ox} (V_{gs} - V_{th})^2 \quad (|V_{ds}| > |V_{gs} - V_{th}|), \quad (2.2)$$

where  $W$  is the channel width,  $L$  is the channel length,  $\mu$  is the mobility and  $C_{ox}$  is the capacitance of the gate dielectric per unit area. From Eq. 2.2 it is obvious that  $\sqrt{I_{ds}}$  is linearly proportional to  $V_{gs}$  and that the slope of this line is proportional to the mobility  $\mu$ . The saturation field-effect mobility can thus easily be extracted from this curve. In addition, extrapolating the linear part of  $\sqrt{I_{ds}}$  to zero current yields the threshold voltage  $V_{th}$ , as shown in Fig. 2.8. Plotting the transfer characteristics on a semi-logarithmic scale allows extraction of two other transistor parameters:  $V_{on}$ , defined as the voltage at which the drain current abruptly increases above a defined low off-current level, and the subthreshold slope,  $S$ , which depends on the gate dielectric capacitance and the trap states at the interface [77].

The total capacitance of the gate dielectric per area can be calculated based on the relative dielectric constant  $\epsilon_r$  and the thickness of the dielectric layer  $t$ . Capacitance-voltage measurements pointed out that the relative dielectric constant of sputtered  $\text{SiO}_2$  is  $\epsilon_r = 5$ , which is somewhat larger than the value obtained for thermally grown  $\text{SiO}_2$  ( $\epsilon_r = 3, 9$ ). The measured  $\epsilon_r$  for P $\alpha$ MS is 2.5.

## 2.2.2 Characterization of OLEDs

The fabricated OLEDs were measured in a  $\text{N}_2$ -filled glovebox using standard probe needles, which were connected to the SMUs of an Agilent 4156C parameter analyzer. Simultaneous to current-voltage measurements the emitted optical power was detected. This was done using a calibrated integrated sphere (SphereOptics Hoffman GmbH). Because of the large sample size and the impossibility to wire-bond our light-emitting devices, the sample was positioned on top of this integrated sphere. This introduced a small error on the measured light intensity. Assuming a Lambertian dependence of the emitted light [241], i.e.  $I = I_0 \cdot \cos \theta$ , a 5% loss of the total optical power of the light-emitting device was calculated. The measured light intensity  $P_{meas}$  is thus only 95% of the actual optical power  $P_{tot}$  of the devices:

$$P_{meas} = 0.95 P_{tot}. \quad (2.3)$$

An additional consequence of this measurement setup is that light which is waveguided in the sample substrate is not taken into account. A photograph of the setup is shown in Fig. 2.9 (left).

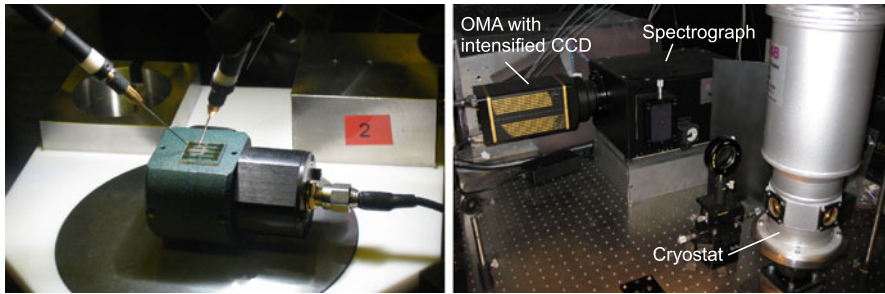


**Fig. 2.9** (Left) Photograph of the setup used to characterize OLEDs, and (right) Photograph of the setup employed to determine the spectral characteristics of OLEDs

To determine the spectral characteristics of our OLEDs, the emitted light was detected by means of an optical multichannel analyzer (OMA) in conjunction with charge coupled device (CCD) (Fig. 2.9 (right)). These measurements were performed at room temperature in a cryostat or by using a small  $N_2$  container to prevent photo-oxidation. The external quantum efficiency  $\eta_{ext}$  could then be calculated based on luminance, electroluminescence spectrum and current.  $\eta_{ext}$  is defined as the number of emitted photons per electron-hole pair injected into the active light-emitting layer, i.e.

$$\eta_{ext} = \frac{P_{tot}/E_{phot}}{I/q}, \quad (2.4)$$

where  $E_{phot}$  is the average photon energy,  $I$  is the injected current and  $q$  is the elementary charge. If  $E_{phot}$  is given in eV, the external quantum efficiency reduces to:

$$\eta_{ext} = \frac{P_{tot}[\text{W}]}{I[\text{A}]E_{phot}[\text{eV}]}. \quad (2.5)$$

The average photon energy  $E_{phot}$  is calculated by:

$$E_{phot} = \frac{\int (hc/\lambda) f(\lambda) d\lambda}{\int f(\lambda) d\lambda}, \quad (2.6)$$

where  $\lambda$  is the wavelength,  $h$  is Planck's constant,  $c$  is the speed of light in free space and  $f(\lambda)$  is the emission spectral distribution. Since the emission spectrum of OLEDs is not always symmetric around the emission peak, this energy often differs from the energy corresponding to the peak emission wavelength.

### 2.2.3 Time-Resolved Photoluminescence Measurements

Time-resolved photoluminescence spectroscopy is a characterization technique where the emission of a sample is monitored as a function of time after excita-

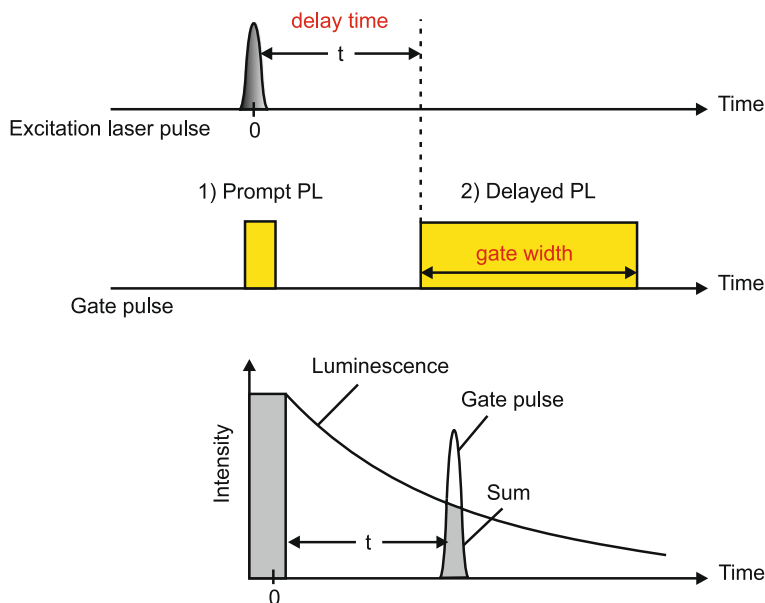


**Fig. 2.10** Principle of time-resolved photoluminescence measurements

tion. This makes it possible to separate prompt fluorescence from delayed emission. Delayed emission originating from the radiative decay of singlets is referred to as delayed fluorescence, whereas the emission from triplets is called phosphorescence. Time-resolved spectroscopy also allows determination of the decay kinetics of light-emitting materials. By recording the emission spectra over a wide range of delay times after the laser pulse excitation, the decay of the emission intensity can be measured. The lifetime of the light-emitting species can then be obtained by fitting this curve. The principle of time-resolved photoluminescence spectroscopy is illustrated in Fig. 2.10.

The setup used at imec to perform time-resolved photoluminescence measurements is depicted in Fig. 2.11. A nitrogen laser (Spectra-Physics) with pulse duration of 4 ns operating at 10 Hz was used for optical excitation at 337 nm. The emission spectra were recorded using a triple-grating monochromator (Acton SpectrPro 2300i) coupled to an intensified CCD camera (PI-MAX from Princeton Instruments) with a time gated, intensified diode array detector, which was synchronized by the electrical trigger of the laser. The detection window could be selected between 1 ns and 25 ms. A variable delay of 75 ns to 25 ms after optical excitation allowed the detection of weak delayed luminescence after the intense prompt fluorescence. The spectra were typically accumulated by averaging over 100 to 300 pulses in order to increase the signal-to-noise ratio. To prevent photo-oxidation the sample was loaded into a temperature regulating nitrogen cryostat, which allowed spectroscopic measurements within a temperature range from 77 K to 350 K. Decay kinetics of phosphorescent materials could be studied using this setup.

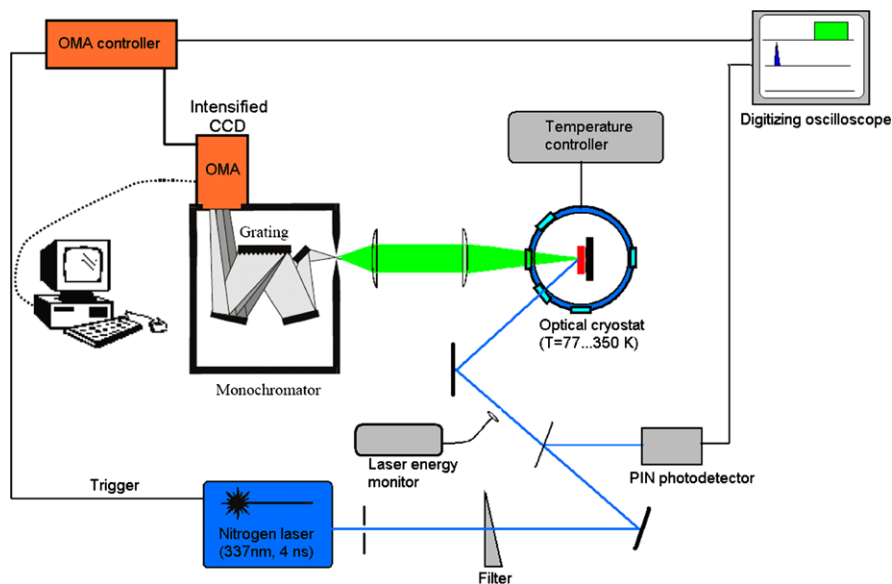
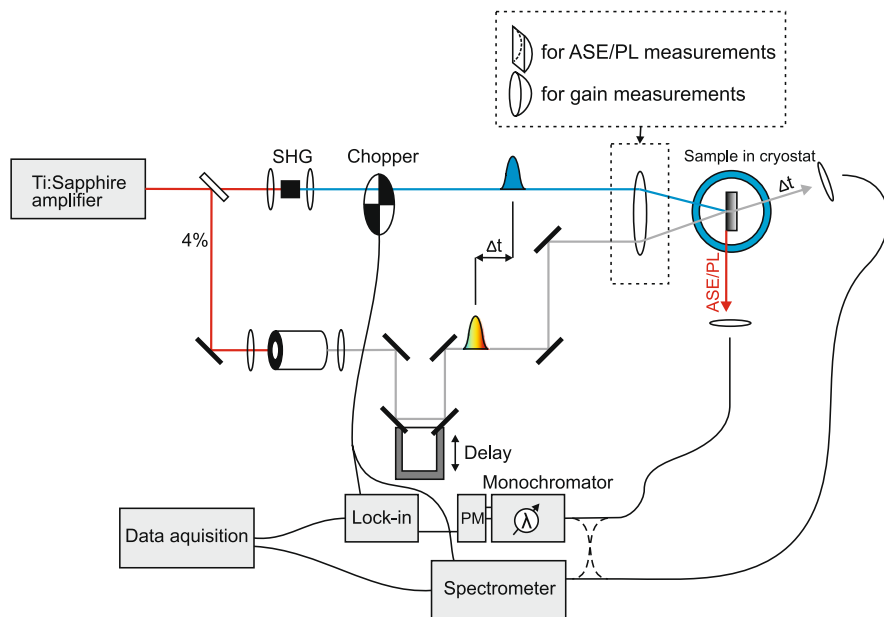


Fig. 2.11 Schematic illustration of the time-resolved photoluminescence measurement setup

### 2.2.4 Time-Resolved Pump-Probe Experiments

As discussed in Chap. 1 (Sect. 1.3.3) transient absorption measurements or time-resolved pump-probe measurements allow ultra-fast measurements of photo-excitations. With this technique the absorbance at a particular wavelength or range of wavelengths of a sample is measured as a function of time after excitation by a fast femtosecond laser pulse (pump laser). Pump and probe experiments are particularly useful to analyze gain in organic compounds. Indeed, at wavelengths where there is gain, the probe beam will be amplified, whereas at wavelengths where competing absorption processes are dominant, the probe beam is attenuated.

Time resolved pump-probe experiments were performed in close collaboration with RWTH in Aachen. The experimental setup realized at RWTH is illustrated in Fig. 2.12. The key component is a femtosecond regenerative Ti:sapphire amplifier (Spectra-Physics Spitfire XP Shortpulse), which allows excitation fluences up to 3 mJ per pulse and delivers a pulse train at a repetition rate of 1 kHz. At the center wavelength of 800 nm the pulse duration was about 35 fs. A beamsplitter splitted this beam into an intense pump beam for optical excitation and a weak probe beam. For efficient optical excitation of the organic films, an ultrathin nonlinear BBO crystal was inserted into the pump beam to generate optical pulses at 400 nm wavelength via second harmonic generation (SHG). The duration of these 400 nm pulses was  $\sim 40$  fs. Furthermore, the pump beam was chopped mechanically at 500 Hz and excited the sample at  $t = 0$ . The excitation spot was circular with a full-width-half-maximum (FWHM) of 400  $\mu\text{m}$  (Gaussian profile) and the pump fluence was determined as the peak value at the center of the pump spot. To prevent photo-oxidation



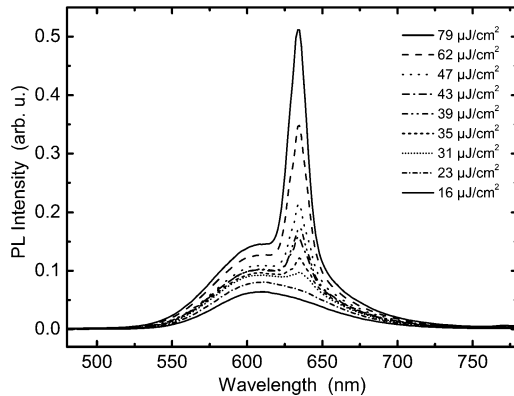
**Fig. 2.12** Experimental setup for ASE/PL- and time resolved pump-probe measurements

during the measurements, the samples were mounted in a cryostat. As can be seen on Fig. 2.12, a fraction of the fundamental laser output was spectrally broadened by a sapphire crystal, delayed by a motorized delay stage and focused on the pump illuminated sample spot. This was the probe beam. The much smaller probe spot (50  $\mu\text{m}$  FWHM) was carefully aligned to the center of the pump spot. The transmitted part of the probe beam was guided by an optical fiber to a monochromator and its intensity was measured by a photomultiplier. A lock-in amplifier was synchronized to the chopper frequency and measured the pump induced transmission change. Typically, the experiments were carried out by changing the wavelength for a particular time delay. Afterwards, the time delay was set to the next value and the measurement was repeated.

### 2.2.5 Amplified Spontaneous Emission and Loss Measurements

Amplified spontaneous emission and loss measurements were performed using the same setup as for time-resolved pump-probe experiments realized at RWTH in Aachen (Fig. 2.12). Only some minor modifications were necessary. The measurements were carried out by collecting and detecting the light emitted from the sample in the optically pumped region. The probe beam was blocked in this case. The pump beam ( $\lambda = 400 \text{ nm}$ ) on the other hand, was elliptically focused on the sample by means of a cylindrical lens, resulting in a narrow excitation stripe. When the

**Fig. 2.13** Emission spectra of Alq<sub>3</sub>:DCM for different laser fluences at 400 nm excitation wavelength (Measurements performed by RWTH Aachen)



pump spot illuminated a region near the edge of the sample, the facet of the organic layer emitted a sufficient amount of light for optical detection. For different average pump powers, the edge-emitted spectrum could then be recorded by guiding the emitted light by an optical fiber to a spectrometer or a monochromator and photomultiplier tube. Similar to the pump-probe measurements, the samples were mounted in a cryostat to prevent degradation and especially photo-oxidation during experiments. Besides, the sample temperature could be controlled in the range from 10 K to room temperature. ASE measurements carried out on a 300-nm thick Alq<sub>3</sub>:DCM film at a concentration of 2% DCM are shown in Fig. 2.13. The obtained spectra clearly indicate the dependence of the spectral emission components on the excitation fluence.

Waveguide losses were analyzed by monitoring the edge-emitted light generated in the organic layer by ASE at different distances between the pump spot and the waveguide edge [168]. Since this technique requires a well-defined pump spot, a slit was inserted in the pump beam path to cut off the tails of the elliptical spot in the elongated direction. The pump spot was gradually moved away from the waveguide edge by translating the sample perpendicularly to the laser beam. Since the output intensity from the end of the excitation stripe is assumed to be constant, the observed decreases in the edge-emitted signal result from waveguide losses (mainly absorption and scattering) within the unpumped region. The waveguide loss coefficient  $\alpha$  could be determined according to

$$I(z) = I_0 \exp(-\alpha z), \quad (2.7)$$

where  $I_0$  is the light intensity at  $z = 0$ .

### 2.2.6 Determination of Thermally Stimulated Luminescence

Thermally stimulated luminescence (TSL) is the phenomenon of luminescent emission after removal of excitation under conditions of increasing temperature. Generally, in the TSL method the trapping states are first populated by photogeneration of

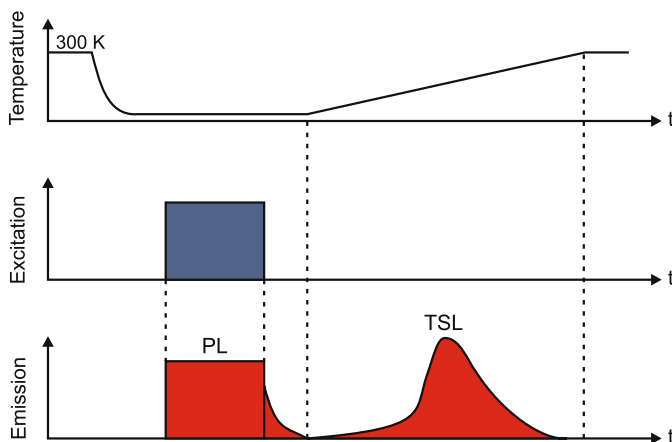


**Fig. 2.14** Measuring procedure of thermally stimulated emission experiments

charge carriers, usually at low temperatures in order to prevent a fast escape. Then, the trapped charge carriers are released by heating up the sample with a linear temperature ramp while the luminescence due to radiative recombination is recorded as a function of temperature. This procedure is illustrated in Fig. 2.14. If an energy distribution of the trap states exists, TSL spectra are a complicated convolution of contributions from different traps at different energies and fractional heating techniques have to be applied, which are based on cycling the sample with a large number of small temperature oscillations superimposed on a constant heating run. Consequently, the TSL is a useful tool for determining the trap depths even when traps are not well separated in energy or are continuously distributed. In addition, TSL also allows analysis of the trap spectra even when they are complex.

TSL measurements were carried out at the National Academy of Science of Ukraine using a home-built setup operable from 4 K to 350 K using a temperature controlled helium cryostat. After cooling down to 4 K, the samples were photo-excited, usually for 30 s, by a high-pressure 500 W mercury lamp with an appropriate set of glass optical filters for light selection. After the photo-excitation, the TSL was detected in a photon-counting mode with a cooled photomultiplier, positioned next to the cryostat window. The TSL measurements were performed either at a constant heating rate of 0.15 K/s or in the fractional heating regime. The latter procedure allows the determination of trap depth when different groups of traps are not well separated in energy or are continuously distributed. A more detailed description of the TSL method is described in literature [242, 243].



Device Architecture and Materials for Organic  
Light-Emitting Devices  
Targeting High Current Densities and Control of the  
Triplet Concentration  
Schols, S.  
2011, XV, 154 p., Hardcover  
ISBN: 978-94-007-1607-0